

Hadron Structure and Form Factors

C. Alexandrou

*Department of Physics, University of Cyprus, P.O. Box 20537, 1678 Nicosia, Cyprus and
Computation-based Science and Technology Research Center, Cyprus Institute, P.O. Box 27456,
1645 Nicosia, Cyprus*
E-mail: alexand@ucy.ac.cy

We review recent results on hadron form factors and nucleon generalized parton distributions obtained with dynamical lattice QCD simulations. We discuss lattice artifacts and open questions, and present the connection of lattice results to hadron structure and to the corresponding quantities measured in experiment.

*The XXVIII International Symposium on Lattice Field Theory, Lattice2010
June 14-19, 2010
Villasimius, Italy*

1. Introduction

Lattice QCD simulations are currently being performed with dynamical degenerate u- and d- quarks with a mass close to their physical value as well as the strange quark, using a number of different discretization schemes with the most common being Wilson-improved, staggered and chiral fermions. Furthermore, simulations at several lattice spacings and volumes are becoming available, enabling a comprehensive study of lattice artifacts. The masses of low-lying hadrons have been computed and extrapolated to the continuum limit using large enough lattice sizes to ensure that volume effects are small [1, 2]. These calculations show agreement with experiment and therefore pave the way for evaluating other phenomenologically interesting quantities beyond these masses.

Several collaborations, using dynamical quarks with pion mass down to about 300 MeV, have calculated the pion electromagnetic (EM) form factor [3], which is obtained from the matrix element $\langle \pi^+(p') | J_\mu | \pi^+(p) \rangle = (p_\mu + p'_\mu) F_\pi(q^2)$, where $q^2 = (p' - p)^2 = -Q^2$. Based on vector dominance, lattice data are fitted to the form $F_\pi(Q^2) = (1 + \langle r^2 \rangle Q^2 / 6)^{-1}$ to extract the mean squared radius, which is shown in Fig. 1. As can be seen, there is an increase in the value of $\langle r^2 \rangle$ at small pion mass, m_π . An accurate extraction of $\langle r^2 \rangle$ benefits from evaluating the form factor at small values of Q^2 accomplished by using twisted boundary conditions (b.c.). In a recent calculation, ETMC combined twisted b.c. and the so called ‘one-end’ trick to incorporate the all-to-all propagator and improve statistics. Using simulations with two degenerate light quarks ($N_f = 2$) at two lattice spacings and two volumes [4] the assessment of cut-off and volume effects was carried out. Lattice results on F_π obtained with pion masses in the range of 300 MeV to 500 MeV, are extrapolated to the physical point using NNLO chiral perturbation theory (PT). The resulting form factor is shown in Fig. 2 [4] and it is in agreement with experiment.

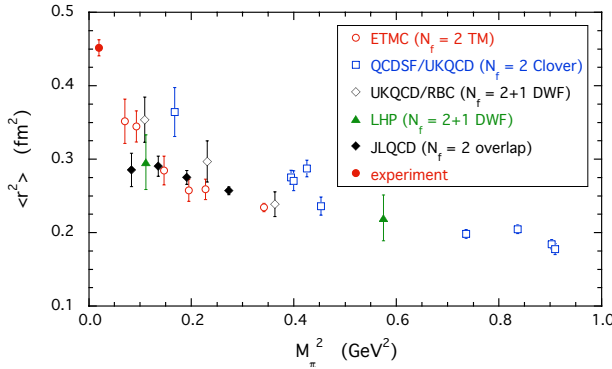


Figure 1: The pion mean square radius as a function of m_π^2 obtained using simulations with $N_f = 2$ twisted mass quarks.

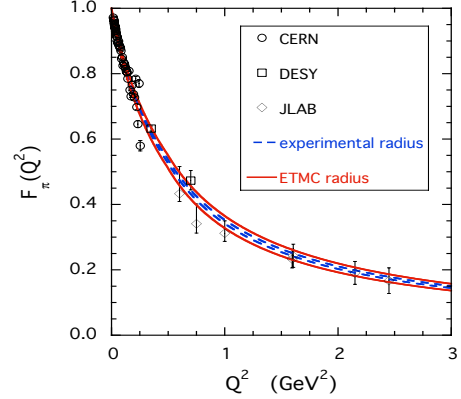


Figure 2: F_π extrapolated to the physical pion mass (red band) using NNLO chiral PT compared to experiment (blue band).

As simulations with quark masses close to the physical value become available, the study of resonances and decays of unstable particles becomes an important issue. The ρ -meson width has been studied by several groups [5]. Considering a $\pi^+\pi^-$ system in the $I = 1$ -channel, the P-wave scattering phase shift $\delta_{11}(k)$ in infinite volume is related via Lüscher’s relation to the energy shift in a finite box. Using $N_f = 2$ twisted mass fermions (TMF) and considering the center of mass frame

and two moving frames one extracts the phase shift at different values of the energy, shown in Fig. 3. From the effective range formula $\tan \delta_{11}(k) = \frac{g_{\rho\pi\pi}^2}{6\pi} \frac{k^3}{E_{CM}(M_R^2 - E_{CM}^2)}$, where $k = \sqrt{E_{CM}^2/4 - m_\pi^2}$ one determines M_R and the coupling $g_{\rho\pi\pi}$ and then extracts the width using $\Gamma_\rho = \frac{g_{\rho\pi\pi}^2}{6\pi} \frac{k_R^3}{M_R^2}$, where $k_R = \sqrt{M_R^2/4 - m_\pi^2}$. The results on the width as a function of m_π^2 are shown in Fig. 4 [6].

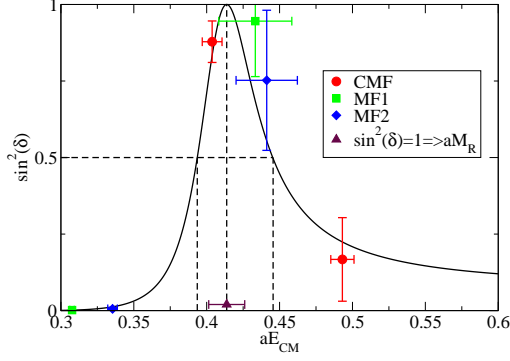


Figure 3: The ρ -meson phase shift at $m_\pi = 308$ MeV for a lattice of $L = 2.8$ fm.

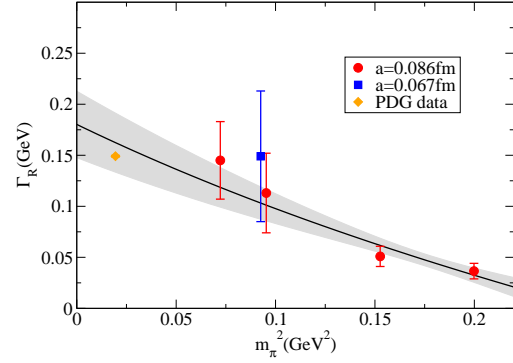


Figure 4: The ρ -meson width for $N_f = 2$ twisted mass fermions as a function of m_π^2 .

Having reproduced the low-lying hadron spectrum [1, 2, 7, 8], the masses of excited states can be studied using e.g. variational methods [9]. Furthermore, one can go beyond masses and consider form factors (FFs) and generalized parton distributions (GPDs) that probe hadron structure. The characterization of nucleon structure, in particular, is considered a milestone in hadronic physics and many experiments have been carried out to measure nucleon FFs and structure functions. Experiments on nucleon FFs started in the 50s. A new generation of experiments using polarized beams and targets are yielding high precision data spanning larger Q^2 ranges. Therefore, nucleon FFs serve as a further benchmark for lattice QCD. FFs provide ideal probes of the charge and magnetization distributions of the hadron as well as a determination of its shape in analogy to similar studies in e.g. deuteron and other nuclei.

Non-relativistically the form factor can be related to the density distribution via

$$F(\vec{q}^2) = \int d^3x e^{-i\vec{q}\cdot\vec{x}} \langle \psi | \rho(\vec{x}) | \psi \rangle.$$

In Fig. 5 we show the intrinsic charge density contours of a spin-zero nucleus showing deformation revealed through measurements of transition densities using electron scattering.

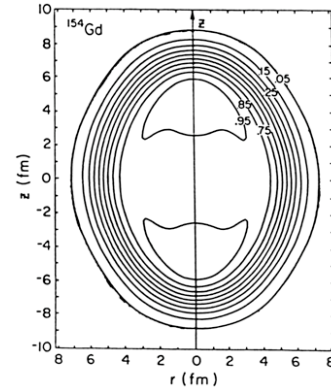


Figure 5: Tomographic view of the zero-spin deformed nucleus ^{154}Gd derived from its rotational bands using electron scattering.

In what follows we will review the status of lattice QCD calculations on baryon form factors and nucleon generalized parton distributions.

2. Nucleon Generalized Form Factors - Definitions

In this section, we briefly define the quantities for which results are presented. High energy scattering can be formulated in terms of light-cone correlation functions. Considering one-particle states $|p'\rangle$ and $|p\rangle$, GPDs are defined by [10, 11]:

$$F_\Gamma(x, \xi, q^2) = \frac{1}{2} \int \frac{d\lambda}{2\pi} e^{i\lambda n} \langle p' | \bar{\psi}(-\lambda n/2) \Gamma \mathcal{P} e^{ig \int_{-\lambda/2}^{\lambda/2} d\alpha n \cdot A(n\alpha)} \psi(\lambda n/2) | p \rangle,$$

where $\bar{P} = (p' + p)/2$, $\xi = -n \cdot q/2$, x is the momentum fraction, and n is a light-cone vector with $\bar{P} \cdot n = 1$.

There are three different types of operators, depending on the choice of Γ .

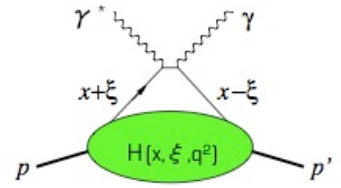
Considering nucleon states these are

$$\Gamma = \not{n} \rightarrow \frac{1}{2} \bar{u}_N(p') \left[\not{n} H(x, \xi, q^2) + i \frac{n_\mu q_\nu \sigma^{\mu\nu}}{2m_N} E(x, \xi, q^2) \right] u_N(p)$$

$$\Gamma = \not{n} \gamma_5 \rightarrow \frac{1}{2} \bar{u}_N(p') \left[\not{n} \gamma_5 \tilde{H}(x, \xi, q^2) + \frac{n \cdot q \gamma_5}{2m_N} \tilde{E}(x, \xi, q^2) \right] u_N(p)$$

$$\Gamma = n_\mu \sigma^{\mu\nu} \rightarrow \text{tensor GPDs}$$

“Handbag” diagram



Expansion of the light cone operator leads to a tower of local twist-2 operators $\mathcal{O}_\Gamma^{\mu\mu_1\ldots\mu_n}$, related to moments. The diagonal proton matrix elements $\langle P | \mathcal{O}_\Gamma(x) | P \rangle$, measured in deep inelastic scattering, are connected to the parton distributions $q(x)$, $\Delta q(x)$, $\delta q(x)$. The twist-2 operators are defined by

$$\mathcal{O}_\not{n}^{\mu\mu_1\ldots\mu_n} = \bar{\psi} \gamma^{\{\mu} i \overleftrightarrow{D}^{\mu_1} \ldots i \overleftrightarrow{D}^{\mu_n\} \psi : \xrightarrow{\text{unpolarized}} \langle x^n \rangle_q = \int_0^1 dx x^n [q(x) - (-1)^n \bar{q}(x)]$$

$$\tilde{\mathcal{O}}_{\not{n} \gamma_5}^{\mu\mu_1\ldots\mu_n} = \bar{\psi} \gamma_5 \gamma^{\{\mu} i \overleftrightarrow{D}^{\mu_1} \ldots i \overleftrightarrow{D}^{\mu_n\} \psi : \xrightarrow{\text{helicity}} \langle x^n \rangle_{\Delta q} = \int_0^1 dx x^n [\Delta q(x) + (-1)^n \Delta \bar{q}(x)]$$

$$\mathcal{O}_{n_\mu \sigma^{\mu\nu}}^{\rho\mu_1\ldots\mu_n} = \bar{\psi} \sigma^{\rho\{\mu} i \overleftrightarrow{D}^{\mu_1} \ldots i \overleftrightarrow{D}^{\mu_n\} \psi : \xrightarrow{\text{transversity}} \langle x^n \rangle_{\delta q} = \int_0^1 dx x^n [\delta q(x) - (-1)^n \delta \bar{q}(x)]$$

where $q = q_\downarrow + q_\uparrow$, $\Delta q = q_\downarrow - q_\uparrow$, $\delta q = q_\top + q_\perp$, and the curly brackets represent a symmetrization over indices and subtraction of traces. The off-diagonal matrix elements extracted from deep virtual Compton scattering can be written in terms of generalized form factors (GFFs), which contain both form factors and parton distributions:

$$\begin{aligned} \langle N(p', s') | \mathcal{O}_\not{n}^{\mu\mu_1\ldots\mu_n} | N(p, s) \rangle = & \bar{u}_N(p', s') \left[\sum_{i=0, \text{even}}^n \left(A_{n+1, i}(q^2) \gamma^{\{\mu} + B_{n+1, i}(q^2) \frac{i \sigma^{\{\mu\alpha} q_\alpha}{2m_N} \right) q^{\mu_1} \ldots q^{\mu_i} \right. \\ & \left. \bar{P}^{\mu_{i+1}} \ldots \bar{P}^{\mu_n\} + \text{mod}(n, 2) C_{n+1, 0}(q^2) \frac{1}{m_N} q^{\{\mu} q^{\mu_1} \ldots q^{\mu_n\}} \right] u_N(p, s) \quad (2.1) \end{aligned}$$

and similarly for $\mathcal{O}_{\not{n} \gamma_5}$ (in terms of $\tilde{A}_{ni}(q^2)$, $\tilde{B}_{ni}(q^2)$) and $\mathcal{O}_{n_\mu \sigma^{\mu\nu}}$ (in terms of A_{ni}^T , B_{ni}^T , C_{ni}^T and D_{ni}^T). We list the following special cases:

- $n = 1$: Ordinary nucleon form factors:

$$\begin{aligned} A_{10}(q^2) = F_1(q^2) &= \int_{-1}^1 dx H(x, \xi, q^2), & B_{10}(q^2) = F_2(q^2) &= \int_{-1}^1 dx E(x, \xi, q^2) \\ \tilde{A}_{10}(q^2) = G_A(q^2) &= \int_{-1}^1 dx \tilde{H}(x, \xi, q^2), & \tilde{B}_{10}(q^2) = G_P(q^2) &= \int_{-1}^1 dx \tilde{E}(x, \xi, q^2), \end{aligned}$$

where in the case of the EM current, $j_\mu = \bar{\psi}(x)\gamma_\mu\psi(x)$, the nucleon matrix element is written in the form $\bar{u}_N(p', s') \left[\gamma_\mu F_1(q^2) + \frac{i\sigma_{\mu\nu}q^\nu}{2m_N} F_2(q^2) \right] u_N(p, s)$. The Dirac F_1 and Pauli F_2 FFs are related to the electric and magnetic Sachs FFs via the relations: $G_E(q^2) = F_1(q^2) - \frac{q^2}{(2m_N)^2} F_2(q^2)$ and $G_M(q^2) = F_1(q^2) + F_2(q^2)$. For the axial vector current $A_\mu^a = \bar{\psi}(x)\gamma_\mu\gamma_5\frac{\tau^a}{2}\psi(x)$ the nucleon matrix element is of the form $\bar{u}_N(p', s') \left[\gamma_\mu\gamma_5 G_A(q^2) + \frac{q_\mu\gamma_5}{2m_N} G_P(q^2) \right] \frac{1}{2}u_N(p, s)$.

• $A_{n0}(0), \tilde{A}_{n0}(0), A_{n0}^T(0)$ are moments of parton distributions, e.g. $\langle x \rangle_q = A_{20}(0)$ and $\langle x \rangle_{\Delta q} = \tilde{A}_{20}(0)$ are the spin independent and helicity distributions. Knowing these quantities one can evaluate the quark spin, $J_q = \frac{1}{2}[A_{20}(0) + B_{20}(0)] = \frac{1}{2}\Delta\Sigma_q + L_q$ and investigate the fraction of the spin carried by quarks and its contribution to the total spin via the nucleon spin sum rule, $\frac{1}{2} = \frac{1}{2}\Delta\Sigma_q + L_q + J_g$, as well as the momentum fraction carried by gluons via the momentum sum rule: $\langle x \rangle_g = 1 - A_{20}(0)$.

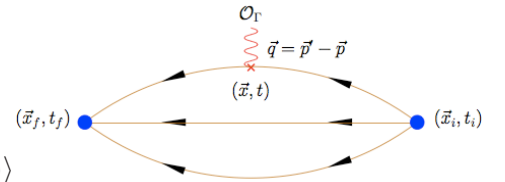
3. Lattice evaluation

In order to extract the matrix elements connected to GFFs we need to evaluate three-point correlators and compute the renormalization of the operators involved. Despite recent progress on the evaluation of disconnected loops, most lattice calculations of GFFs do not take into account disconnected contributions. Therefore, in what follows, we consider iso-vector operators for which such contributions are zero in the isospin limit. For one-derivative operators, mixing with lower dimension operators is avoided by symmetrizing over the Lorentz indices and making them traceless. The study of cut-off and finite volume effects in a systematic way has just begun for baryon GFFs. These are more difficult to assess since chiral expansions that describe such dependencies are not as developed as in the light meson case. The presence of more uncertainties in the chiral expansion combined with the larger statistical noise, which for the nucleon two-point function increases like $\frac{\text{noise}}{\text{signal}} \sim e^{(m_N - 3m_\pi/2)}/\sqrt{N}$, make the extrapolation of these quantities to the physical point much more demanding. In this review we will focus on: i) Nucleon form factors and lower moments using dynamical simulations with pion mass $m_\pi \lesssim 500$ MeV and spatial lattice length $L \gtrsim 2$ fm and ii) the N - Δ system in order to determine the complete set of coupling constants needed in chiral expansions. Other topics relevant to hadron structure, such as the strange nucleon FFs, hyperon, Roper and nucleon negative parity FFs, distribution amplitudes and transverse momentum dependent parton distributions can be found in Ref. [12] and in contributions to this volume.

• **Three-point functions:** For the extraction of matrix elements of local operators we need the evaluation of two-point and three-point functions defined by

$$G(\vec{p}, t) = \sum_{\vec{x}_f} e^{-i\vec{x}_f \cdot \vec{p}} \Gamma_{\beta\alpha}^4 \langle J_\alpha(\vec{x}_f, t_f) \bar{J}_\beta(0) \rangle$$

$$G^{\mu\nu}(\Gamma, \vec{p}', \vec{q}, t) = \sum_{\vec{x}_f, \vec{x}} e^{i\vec{x} \cdot \vec{q}} e^{-i\vec{x}_f \cdot \vec{p}'} \Gamma_{\beta\alpha} \langle J_\alpha(\vec{x}_f, t_f) \mathcal{O}^{\mu\nu}(\vec{x}, t) \bar{J}_\beta(\vec{x}_i, t_i) \rangle$$



Only the displayed connected diagram is evaluated, which, for most current applications, is done by using sequential inversion “through the sink” fixing the sink-source separation $t_f - t_i$, final momentum \vec{p}' and Γ - projection matrices. Smearing techniques are crucial for improving ground state dominance in three-point correlators and thus keep $t_f - t_i$ as short as possible. We stress that it is important to ensure that the time separation $t_f - t_i$ used is sufficiently large by performing the

calculation at a bigger time separation and checking the consistency of the results. The generalized eigenvalue method can further improve identification of the ground state [13] and enlarge the upper range of accessible Q^2 -values [14].

• **Renormalization constants:** Most collaborations use non-perturbative renormalization. Using a momentum dependent source [15] one evaluates

$$S^u(p) = \frac{a^8}{V} \sum_{x,y} e^{-ip(x-y)} \langle u(x) \bar{u}(y) \rangle, \quad G(p) = \frac{a^{12}}{V} \sum_{x,y,z,z'} e^{-ip(x-y)} \langle u(x) \bar{u}(z) \mathcal{J}(z,z') d(z') \bar{d}(y) \rangle \quad (3.1)$$

with the amputated vertex functions given by $\Gamma(p) = (S^u(p))^{-1} G(p) (S^d(p))^{-1}$ and \mathcal{J} determines the operator, e.g. $\mathcal{J}(z,z') = \delta_{z,z'} \gamma^\mu \overleftrightarrow{D}^\nu$ would correspond to the local vector current. The Z -factors can be determined in the RI'-MOM scheme by imposing the following conditions

$$Z_q = \frac{1}{12} \text{Tr}[(S(p))^{-1} S^{(0)}(p)] \Big|_{p^2=\mu^2}, \quad Z_q^{-1} Z_{\mathcal{O}} \frac{1}{12} \text{Tr}[\Gamma_{\mu\nu}(p) \Gamma_{\mu\nu}^{(0)-1}(p)] \Big|_{p^2=\mu^2} = 1, \quad (3.2)$$

to extract the renormalization factors Z_q and $Z_{\mathcal{O}}$. These conditions are imposed in the massless theory and therefore a chiral extrapolation is needed. The mass-dependence is very weak for the vector and axial vector operators. This is demonstrated in Fig. 6 for the case of the one-derivative vector the axial-vector operators using $N_f = 2$ TMF [16]. Results on Z_V and Z_A as a function of $(ap)^2$ are shown in Fig. 7 where plateaux are improved after subtracting $\mathcal{O}(a^2)$ -terms perturbatively [17]. Using the RI'-MOM scheme but with a momentum independent source, the RBC-UKQCD Collaborations made a comparison between perturbative and non-perturbative determination of the renormalization constants and found that results for $\langle x \rangle_{u-d}$ [18] with perturbative renormalization are lower bringing them in agreement with LHPC's results, which used perturbative renormalization [19]. It is therefore important to compute the renormalization constants non-perturbatively.

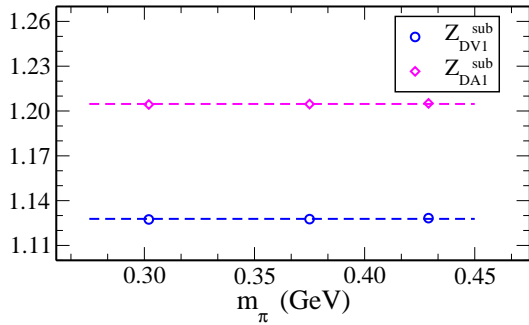


Figure 6: Mass dependence of the renormalization constant for vector and axial vector one-derivative operators for $N_f = 2$ TMF [16].

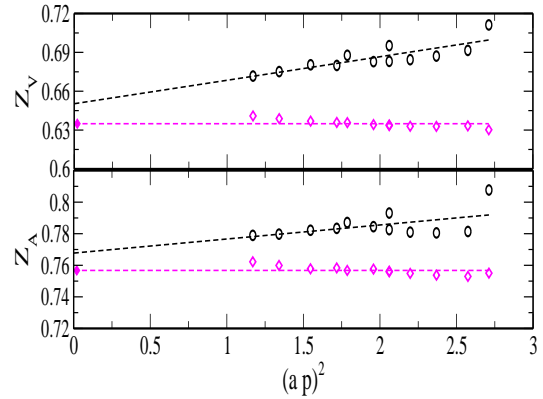


Figure 7: Z_V and Z_A with perturbative subtraction of $\mathcal{O}(a^2)$ -terms for $N_f = 2$ TMF [17].

• **Cut-off effects:** The nucleon axial charge g_A , the isovector momentum fraction $\langle x \rangle_{u-d} = A_{20}(0)$ and helicity fraction $\langle x \rangle_{\Delta u - \Delta d} = \tilde{A}_{20}(0)$ are calculated directly at $Q^2 = 0$ requiring no fits. We can examine their dependence on the lattice spacing by obtaining these quantities at a given

value of the pseudoscalar mass in units of r_0 . In Fig. 8 we show results at three lattice spacings using $N_f = 2$ TMF. As can be seen, $\mathcal{O}(a^2)$ -terms are small and, allowing a linear dependence, yields consistent results to those obtained with a constant fit. This is also true for the nucleon isovector anomalous moment κ_v , Dirac and Pauli radii r_1^2 and r_2^2 that require fits to the EM form factors.

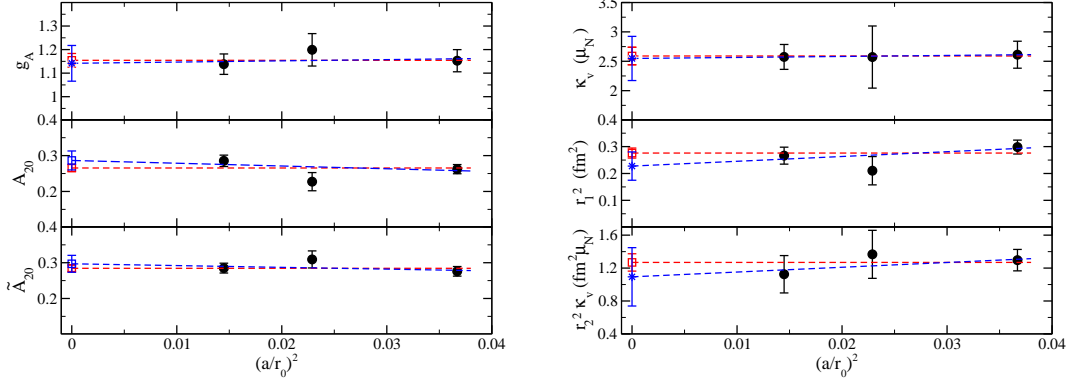


Figure 8: Left: g_A , $\langle x \rangle_{u-d}$, and $\langle x \rangle_{\Delta u-\Delta d}$; Right: the nucleon anomalous magnetic moment κ_v , the Dirac radius r_1^2 and Pauli radius r_2^2 times κ_v as a function of $(a/r_0)^2$. The red line is the result of fitting to a constant; the blue one is a linear fit. The results are obtained using $N_f = 2$ TMF [20].

We therefore conclude that cut-off effects are small for $a < 0.1$ fm for $\mathcal{O}(a)$ -improved actions and that one can use continuum chiral perturbation theory to extrapolate to the physical limit.

• **Finite volume corrections:** In Fig. 9 we compare results on g_A , $\langle x \rangle_{u-d}$ and $\langle x \rangle_{\Delta u-\Delta d}$ computed on different lattice sizes as a function of m_π^2 .

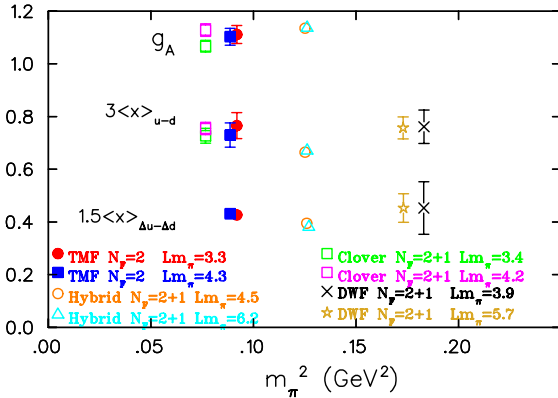


Figure 9: g_A , $3\langle x \rangle_{u-d}$ and $\frac{3}{2}\langle x \rangle_{\Delta u-\Delta d}$ using TMF [20], Clover [21], hybrid [19] and DWF [18].

The observations are: i) Accurate lattice data by LHPC using domain wall valence quarks on staggered sea (hybrid) for $m_\pi \sim 350$ MeV with $Lm_\pi = 4.5$ and $Lm_\pi = 6.2$ show no volume effects; ii) TMF results for $m_\pi \sim 300$ MeV with $Lm_\pi = 3.3$ and $Lm_\pi = 4.3$ are consistent; iii) Results for $\langle x \rangle_{u-d}$ using Clover fermions from QCDSF for $m_\pi \sim 270$ MeV with $Lm_\pi = 3.4$ and $Lm_\pi = 4.2$ are consistent, whereas g_A differs by about a standard deviation; iv) RBC-UKQCD results with domain wall fermions (DWF) with $Lm_\pi = 3.9$ and $Lm_\pi = 5.7$ show no volume effects for $\langle x \rangle_{u-d}$ and $\langle x \rangle_{\Delta u-\Delta d}$ [18].

Within the current statistical uncertainties this comparison, therefore shows that volume effects on $\langle x \rangle_{u-d}$ and $\langle x \rangle_{\Delta u-\Delta d}$ are negligible for $Lm_\pi \gtrsim 3.3$. For g_A volume effects of about one standard deviation are seen for $Lm_\pi \sim 3.4$ and pion mass below 300 MeV and therefore larger lattices keeping $Lm_\pi \gtrsim 4$ may be needed.

Comparing the isovector nucleon EM FFs as a function of Q^2 at $m_\pi \sim 300$ MeV we also find consistent results for $Lm_\pi = 3.3$ and $Lm_\pi = 4.3$. A similar behavior is also observed for the nucleon axial FF $G_A(Q^2)$ whereas the induced pseudoscalar FF $G_p(Q^2)$, which has a pion pole behavior, may suffer from larger finite volume corrections at low Q^2 -values [22].

4. Results on nucleon form factors

Having examined cut-off and volume effects we compare results from various collaborations computed with dynamical fermions for $a \lesssim 0.1 \text{ fm}^1$ and $Lm_\pi \gtrsim 3.3$.

• **Nucleon axial charge:** The axial charge is well known experimentally. Since it is determined at $Q^2 = 0$ there is no ambiguity associated with fitting the Q^2 -dependence of the FF. In Fig. 10 we show recent lattice results using TMF, DWF and a hybrid action of DWF on a staggered sea, all of which are renormalized non-perturbatively. As can be seen, there is a nice agreement among different lattice discretizations and no significant dependence on the quark mass down to about $m_\pi = 260 \text{ MeV}$.

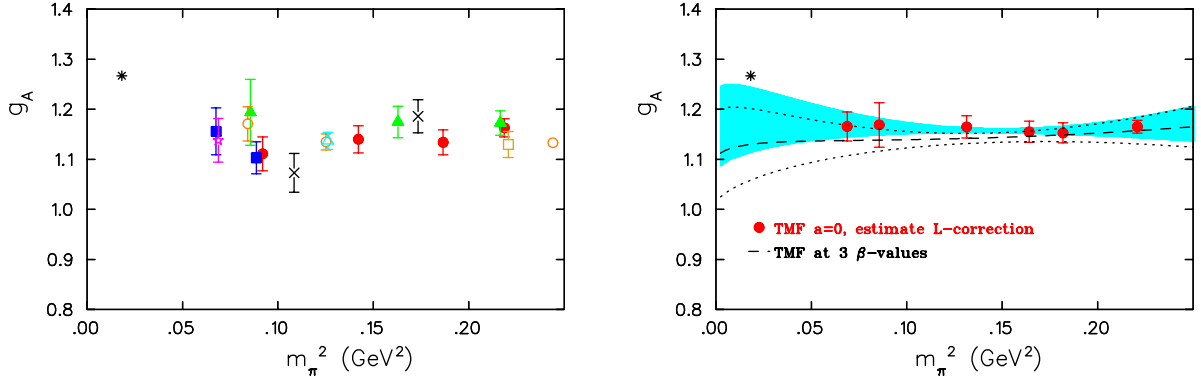


Figure 10: Left: Lattice data on g_A using $N_f = 2$ TMF [20] ($a = 0.089 \text{ fm}$: filled red circles for $L = 2.1 \text{ fm}$ and filled blue squares for $L = 2.8 \text{ fm}$; $a = 0.070 \text{ fm}$: filled green triangles for $L = 2.2 \text{ fm}$; $a = 0.056 \text{ fm}$: purple star for $L = 2.7 \text{ fm}$ and open yellow square for $L = 1.8 \text{ fm}$), $N_f = 2 + 1$ DWF [23] (crosses for $a = 0.114 \text{ fm}$ and $L = 2.7 \text{ fm}$) and $N_f = 2 + 1$ using DWF and staggered sea [19] ($a = 0.124 \text{ fm}$: open orange circles for $L = 2.5 \text{ fm}$ and open cyan triangle for $L = 3.5 \text{ fm}$). The physical point is shown by the asterisk. Right: Volume corrected TMF results extrapolated to the continuum limit together with the fit using HB χ PT (blue band). The band bounded by the lines is the resulting fit to the TMF data shown on the left.

To illustrate the size of lattice artifacts and obtain a value of g_A at the physical point, we use TMF results [22]. The volume corrected [24] data are extrapolated to $a = 0$ using three lattice spacings, namely $a = 0.089 \text{ fm}$, 0.070 fm and 0.056 fm , at two values of the pseudoscalar mass, by fitting to a constant. For intermediate masses we use data at the two coarser lattices. The continuum volume-corrected results are shown in Fig. 10. Chiral extrapolation using one-loop heavy baryon chiral perturbation theory (HB χ PT) in the small scale expansion (SSE) [25] with three fit parameters produces a value of $g_A = 1.12(8)$ at the physical point, which is lower than the experimental value by about a standard deviation. The large error is due to the strong correlation between the Δ axial charge $g_{\Delta\Delta}$ and the counter-term involved in the fit. Therefore, a lattice determination of $g_{\Delta\Delta}$ will allow a more controlled chiral extrapolation. Fitting the raw lattice data produces the band shown by the dotted lines. Therefore one observes that, although the continuum volume-corrected results are closer to experiment, the largest uncertainty is due to the chiral extrapolation and at the physical point the values obtained using the raw and continuum volume-corrected lattice data are consistent.

¹We note that results by the LHPC using a hybrid action have $a = 0.124 \text{ fm}$.

• Nucleon form factors: Recent lattice results on the EM isovector and axial FFs are shown in Fig. 11. We observe a nice agreement among lattice results, in particular for $G_E(Q^2)$ and $G_A(Q^2)$. However, both $G_E(Q^2)$ and $G_A(Q^2)$ decrease with Q^2 less rapidly than experiment. We note that a good description of the Q^2 –dependence for both $G_E(Q^2)$ and $G_M(Q^2)$ is provided by a dipole form using the lattice-computed ρ –meson mass. Lattice results on $G_p(Q^2)$ using TMF and those obtained using the hybrid action on a larger volume, are not consistent, in particular at small Q^2 where $G_p(Q^2)$ increases rapidly due to the pion-pole behavior. From the observed quark mass dependence of $G_p(Q^2)$ [22] the 50 MeV difference in the pion mass may not be sufficient to fully account for this discrepancy, which may indicate volume effects.

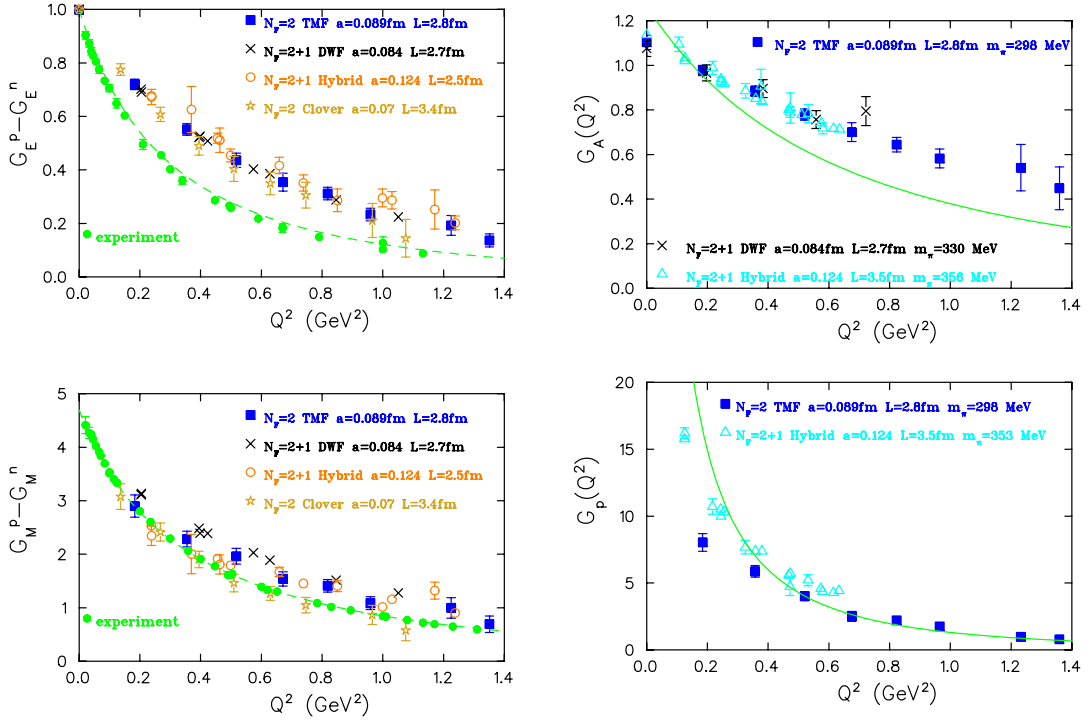


Figure 11: Left: Isovector electric and magnetic nucleon FFs at $m_\pi \sim 300$ MeV using TMF [20] (filled blue squares) DWF [26] (crosses), hybrid [19] (open orange circles) and Clover fermions [27] (yellow stars). Experimental data are shown with the filled green circles accompanied with Kelly's parametrization shown with the dashed line. Right: Axial nucleon FFs. The solid line is a dipole fit to experimental data for $G_A(Q^2)$ combined with pion pole dominance to get the solid curve shown for $G_p(Q^2)$.

Using HB χ PT to one-loop, with Δ degrees of freedom and iso-vector N - Δ coupling included in LO [28] we perform a fit to $F_1(m_\pi, Q^2)$ and $F_2(m_\pi, Q^2)$ with five parameters, namely the iso-vector magnetic moment at the chiral limit κ_V^0 , the isovector and axial N to Δ coupling constants and two counterterms. As can be seen, the chiral extrapolation increases the value of F_1 and F_2 at low Q^2 , bringing it into qualitative agreement with experiment. Application of twisted b.c. with a study of the associated volume corrections [29] will be very useful in enabling us to obtain these FFs at lower Q^2 -values, permitting a better chiral extrapolation. Using the parameters extracted from the fits to F_1 and F_2 we obtain the chiral dependence of the isovector nucleon anomalous magnetic

moment and the Dirac and Pauli radii shown in Fig. 12.

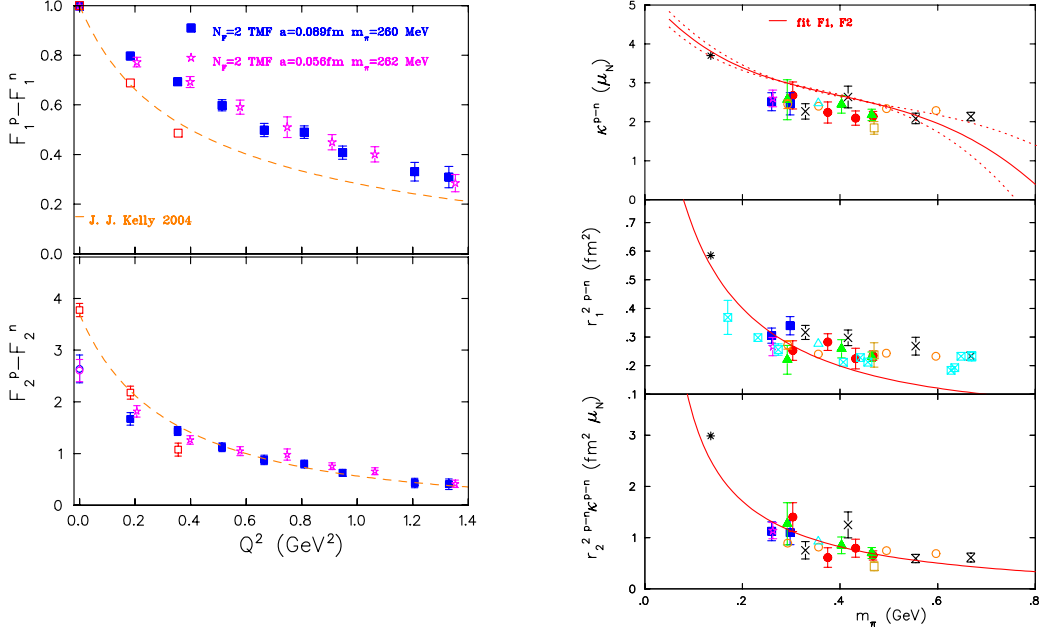


Figure 12: Left: Open squares show the chirally extrapolated results at the physical point. The dashed line is Kelly's parametrization of the experimental data. Right: The solid lines show the prediction of HB χ PT using the parameters obtained from fitting $F_1(m_\pi, Q^2)$ and $F_2(m_\pi, Q^2)$. The notation is the same as that of Fig. 10. For r_1^2 results using Clover fermions [21] are also shown with the cyan cross-in-square symbols.

5. Results on nucleon moments

In this section we show results on the nucleon matrix element of the one-derivative operators $\bar{u}\gamma_{\{\mu} \overleftrightarrow{D}_{\nu\}} u - \bar{d}\gamma_{\{\mu} \overleftrightarrow{D}_{\nu\}} d$ and $\bar{u}\gamma_5\gamma_{\{\mu} \overleftrightarrow{D}_{\nu\}} u - \bar{d}\gamma_5\gamma_{\{\mu} \overleftrightarrow{D}_{\nu\}} d$ in the \overline{MS} scheme at a scale $\mu = 2$ GeV.

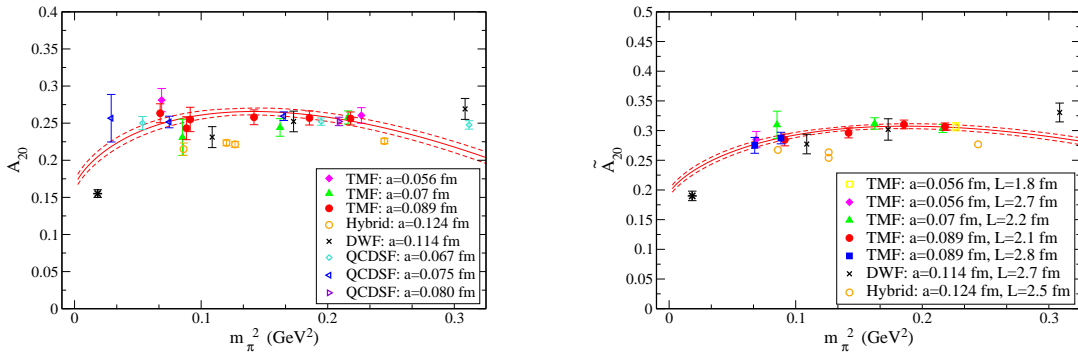


Figure 13: Recent results on the isovector $A_{20} = \langle x \rangle_{u-d}$ and $\tilde{A}_{20} = \langle x \rangle_{\Delta u - \Delta d}$.

In Fig. 13 we compare recent results from ETMC [30], RBC-UKQCD [18], QCDSF [21] and LHPC [19] on the spin-independent and helicity quark distributions. All collaborations except LHPC use non-perturbatively computed renormalization constants. As already mentioned, The

ETMC has, in addition, subtracted $\mathcal{O}(a^2)$ terms perturbatively to reduce lattice artifacts [16]. There is a spread in the values of the lattice results. It was noted that taking a renormalization free ratio leads to a better agreement among lattice data with $Lm_\pi > 4$ [31]. In particular this brought the LHPC data in agreement with those from ETMC and QCDSF.

In HB χ PT [32] the expressions for the m_π -dependence of A_{20} and \tilde{A}_{20} are given by:

$$\langle x \rangle_{u-d} = C \left[1 - \frac{3g_A^2 + 1}{(4\pi f_\pi)^2} m_\pi^2 \ln \frac{m_\pi^2}{\lambda^2} \right] + \frac{c_8(\lambda^2)m_\pi^2}{(4\pi f_\pi)^2}, \quad \langle x \rangle_{\Delta u - \Delta d} = \tilde{C} \left[1 - \frac{2g_A^2 + 1}{(4\pi f_\pi)^2} m_\pi^2 \ln \frac{m_\pi^2}{\lambda^2} \right] + \frac{\tilde{c}_8(\lambda^2)m_\pi^2}{(4\pi f_\pi)^2}$$

Using $\lambda^2 = 1 \text{ GeV}^2$ and the TMF results we obtain the curves shown in Fig. 13, which yield a value higher than experiment for both observables. The very recent result by QCDSF [21] at $m_\pi \sim 170 \text{ MeV}$ remains higher than experiment and highlights the need to understand such deviations.

6. N - Δ system

• **$N\gamma^* \rightarrow \Delta$ form factors:** There is an extensive experimental program to study the N to Δ EM transition and in particular to obtain accurate results on the sub-dominant quadrupole FFs $G_{E2}^*(q^2)$ and $G_{C2}^*(q^2)$ that probe deformation. The experimental results, shown in Fig. 14, are compatible with the blue band obtained assuming deformation in the N - Δ and incompatible with the red band that includes no deformation. These FFs can be computed within lattice QCD and since no disconnected contributions are involved they provide yet another benchmark for lattice methods. The matrix element for N to Δ EM transition is written in terms of three Sachs FFs as:

$$\langle \Delta(p', s') | j^\mu | N(p, s) \rangle = i\mathcal{A} \bar{u}_{\Delta, \sigma}(p', s') \left[G_{M1}^*(Q^2) K_{M1}^{\sigma\mu} + G_{E2}^*(Q^2) K_{E2}^{\sigma\mu} + G_{C2}^*(Q^2) K_{C2}^{\sigma\mu} \right] u_N(p, s),$$

where $\mathcal{A} = \sqrt{\frac{2}{3}} (m_N m_\Delta / E_\Delta(\vec{p}') E_N(\vec{p}))^{1/2}$ is a kinematical factor.

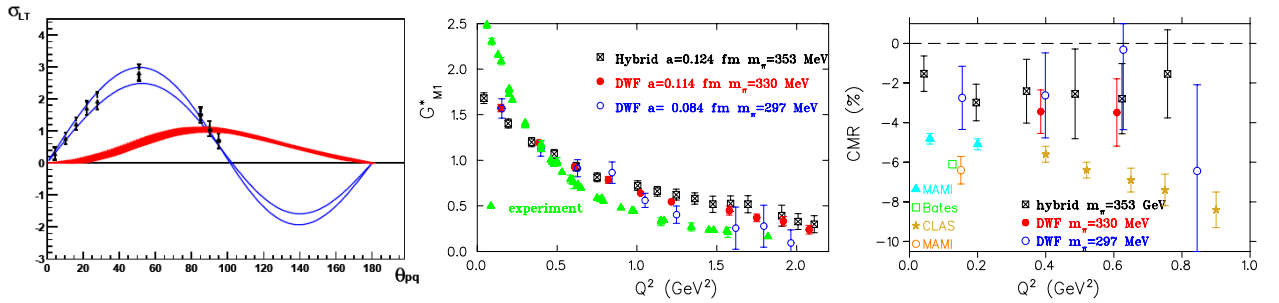


Figure 14: N to Δ EM transition: Left: The transverse-longitudinal response function σ_{LT} vs c.m. angle between p and γ^* (from MAMI and Bates) [33]; The N to Δ magnetic dipole FF (middle) and the ratio of Coulomb quadrupole to magnetic dipole FF (right) for the hybrid action and $N_f = 2 + 1$ DWF.

The extraction of the sub-dominant quadrupole FFs is enabled by constructing optimized sources that isolate G_{E2}^* and G_{C2}^* [34]. In Fig. 14 we show results using a hybrid action of DWF on staggered sea as well as $N_f = 2 + 1$ DWF, provided by RBC-UKQCD. For the dominant dipole FF G_{M1}^* , like for the nucleon FFs, we observe a weaker Q^2 -dependence as compared to experiment,

that again highlights the need of studying these FFs using simulations with $m_\pi < 300$ MeV. Lattice results, shown in Fig. 14 for the ratio of the Coulomb quadrupole to the magnetic dipole FF are non-zero. This is also true for the electric quadrupole FF, pointing to a deformation of the N - Δ .

• **Weak N to Δ transition:** In contrast to the EM transition, the weak N to Δ is not well studied experimentally. Therefore a lattice determination of the axial vector N to Δ FFs would provide important input for phenomenology and in particular for chiral perturbation expansions. The weak N to Δ matrix element $\langle \Delta(p', s') | A_\mu^3 | N(p, s) \rangle = \bar{u}_\Delta^\lambda(p', s') \mathcal{O}_{\lambda\mu} u_N(p, s)$ with

$$\mathcal{O}_{\lambda\mu} = i\mathcal{A} \left[\left(\frac{C_3^A(Q^2)}{m_N} \gamma^\nu + \frac{C_4^A(Q^2)}{m_N^2} p^\nu \right) (g_{\lambda\nu} g_{\rho\nu} - g_{\lambda\rho} g_{\mu\nu}) q^\rho + C_5^A(Q^2) g_{\lambda\mu} + \frac{C_6^A(Q^2)}{m_N^2} q_\lambda q_\mu \right],$$

where $C_5^A(Q^2)$ is the equivalent of the nucleon FF $G_A(Q^2)$ and $C_6^A(Q^2)$ of $G_p(Q^2)$ showing a pion pole behavior [34]. In Fig. 15 we show results on the dominant FFs C_5^A and C_6^A obtained using the hybrid action at $m_\pi \sim 350$ MeV and with $N_f = 2 + 1$ DWF at $m_\pi \sim 330$ MeV and $m_\pi = 300$ MeV.

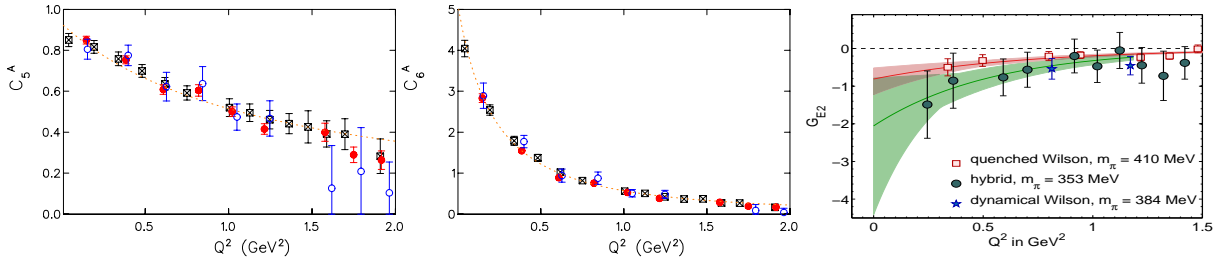


Figure 15: Left and middle: Axial N to Δ FFs C_5^A and C_6^A respectively. The squares are for the hybrid action at $m_\pi \sim 350$ MeV, the filled red circles for DWF at $m_\pi \sim 330$ MeV and the open blue circles for DWF at $m_\pi = 300$ MeV. Right: Δ electric quadrupole FF for quenched, $N_f = 2$ Wilson and $N_f = 2 + 1$ hybrid action.

7. Δ electromagnetic form factors and structure

Experimentally the Δ FFs are very difficult to measure due to the fact that the Δ decays strongly. Only its magnetic moment is measured experimentally albeit with a large error. Therefore lattice calculations can complement experiment by providing these FFs.

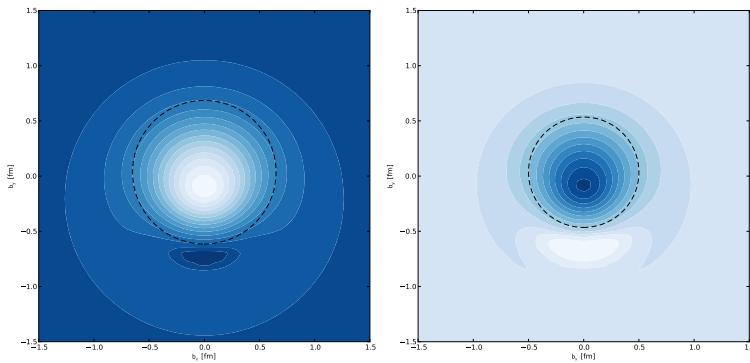


Figure 16: Quark transverse charge densities in the Δ^{++} (left) and Ω^- (right) for the 3/2-spin projection along the x-axis. Darker colors denote smaller values and the charge of the particle is taken into account. A dotted circle of radius 0.5 fm is included for comparison.

The matrix element $\langle \Delta(p', s') | j^\mu(0) | \Delta(p, s) \rangle = \bar{u}_{\Delta,\alpha}(p', s') \mathcal{O}^{\alpha\mu\beta} u_{\Delta,\beta}(p, s)$ can be written as

$$\mathcal{O}^{\alpha\mu\beta} = -\mathcal{A}_\Delta \left\{ \left[F_1^*(Q^2) g^{\alpha\beta} + F_3^*(Q^2) \frac{q^\alpha q^\beta}{(2m_\Delta)^2} \right] \gamma^\mu + \left[F_2^*(Q^2) g^{\alpha\beta} + F_4^*(Q^2) \frac{q^\alpha q^\beta}{(2m_\Delta)^2} \right] \frac{i\sigma^{\mu\nu} q_\nu}{2m_\Delta} \right\}$$

with e.g. the quadrupole FF given by: $G_{E2} = (F_1^* - \tau F_2^*) - \frac{1}{2}(1 + \tau)(F_3^* - \tau F_4^*)$, where $\tau \equiv Q^2/(4m_\Delta^2)$. Optimized sources are constructed to isolate the quadrupole FF G_{E2} , which probes deformation. The transverse charge density of a Δ polarized along the x-axis can be defined in the infinite momentum frame. Using G_{E2} we can predict the ‘shape’ of Δ . The result is shown in Fig. 16 and for spin projection 3/2 it is elongated along the spin axis. The Ω^- shows a similar but smaller deformation [35]. The weak Δ FFs can be computed in an analogous manner [36].

8. Conclusions

The nucleon EM form factors provide a benchmark for lattice QCD beyond hadron masses. Most collaborations obtain results for the isovector FFs up to about $Q^2 = 2 \text{ GeV}^2$. Systematic studies of lattice artifacts on GFFs are now under way and recent data reveal that cut-off effects are negligible for $a \lesssim 0.1 \text{ fm}$, whereas finite volume corrections, although difficult to evaluate, are within the current statistical errors of $\sim (2 - 3)\%$ for $Lm_\pi \gtrsim 3.3$. A possible exception is G_p at low Q^2 -values. We find that, in general, lattice results using different discretization schemes are consistent but they show a milder Q^2 -dependence as compared to experiment. As illustrated in the case of the nucleon axial charge, the biggest uncertainty in comparing with experiment is the chiral extrapolation. Therefore a lattice determination of a number of couplings used as input in chiral extrapolations will enable global fits to e.g. the N - Δ system that can help extrapolation to the physical point. Interesting questions such as the ‘shape’ of a hadron can be addressed using input from lattice form factors as demonstrated for the Δ and Ω . Moments of GPDs yield more detailed information on both longitudinal and transverse distributions and a tomography of hadrons can be obtained by studying these quantities. We therefore, conclude that, overall, there is good progress in baryon structure calculations and that we now are in an exciting era, having simulations close enough to the physical point, in order to probe interesting dynamics in hadronic systems.

Acknowledgments: I would like to thank the members of the ETM collaboration and in particular M. Brinet, J. Carbonell, M. Constantinou, V. Drach, P. A. Harraud, K. Jansen, T. Korzec, M. Papinutto and O. Pene, my long-term collaborators G. Koutsou, J. W. Negele, and A. Tsapalis as well as Y. Proestos and M. Vanderhaeghen for their valuable input on the topics presented. This work was performed using HPC resources from GENCI (IDRIS and CINES) Grant 2009-052271, the Blue-Gene/P at JSC and was partly supported through funding received by the Cyprus Research Promotion Foundation under contracts EPYAN/0506/08, KY-Γ/0907/11, TECHNOLOGY/ΘΕΠΠΣ/0308(BE)/17 and ΔΙΕΘΝΗΣ/ΣΤΟΧΟΣ/0308/07.

References

- [1] St. Dürr *et al.* (BMW), Science 322, 1224 (2008).
- [2] C. Alexandrou *et al.* (ETMC), Phys. Rev. D **80**, 114503 (2009).
- [3] T. Kaneko *et al.* (JLQCD), PoS **LAT2007**, 148 (2007); A. Jüttner *et al.* (RBC-UKQCD), PoS C **D09** (2009) 010; D. Brömmel *et al.* (QCDSF-UKQCD) Eur. Phys. J. C **51**, 335 (2007); D. Brömmel *et al.* (QCDSF), Eur. Phys. J. C **51**, 335 (2007); F. D. R. Bonnet *et al.*, Phys. Rev. D. **72**, 054506 (2005).
- [4] R. Frezzotti, V. Lubicz and S. Simula, Phys. Rev. D **79**, 074506 (2009).

- [5] J. Frison *et al.*, arXiv:1011.3413; S. Aoki *et al.* (PACS-CS), arXiv:1011.1063; S. Aoki *et al.*, Phys. Rev. D **76**, 094506 (2007); M. Göckeler *et al.* (QCDSF), PoS **LATTICE2008**, 136 (2008).
- [6] X. Feng, K. Jansen and D. B. Renner, arXiv:0910.4871; arXiv:1011.5288.
- [7] A. Waker-Loud *et al.* (LHPC), Phys. Rev. D **79** 054502 (2009).
- [8] S. Aoki *et al.* (PACS-CS), Phys. Rev. D **79**, 034503 (2009).
- [9] J. M. Bulava *et al.*, Phys. Rev. D **79**, 034505 (2009); M. S. Mahbub *et al.*, Phys. Lett. B **679**, 418 (2009); G. Engel, *et al.*, arXiv:0910.2802 [hep-lat].
- [10] M. Diehl, Phys. Rep. 388, 41 (2003).
- [11] X. Ji, J. Phys. G24, 1181 (1998).
- [12] J. M. Zanotti, PoS **LATTICE2008**, 007 (2008).
- [13] B. Blossier, M. Della Morte, G. von Hippel, T. Mendes and R. Sommer, JHEP **0904**, 094 (2009).
- [14] H.-W. Lin *et al.*, arXiv:1005.0799
- [15] M. Göckeler *et al.* (QCDSF), Nucl. Phys. **B544**, 699 (1999).
- [16] C. Alexandrou, M. Constantinou, T. Korzec, H. Panagopoulos and F. Stylianou, arXiv:1006.1920.
- [17] C. Alexandrou, M. Constantinou, T. Korzec, H. Panagopoulos and F. Stylianou, PoS **Lattice 2010**, 224 (2010); in preparation.
- [18] Y. Aoki *et al.* (RBC-UKQCD), Phys. Rev. D **82**, 014501 (2010).
- [19] J. D. Bratt *et al.* (LHPC), arXiv:1001.3620.
- [20] C. Alexandrou *et al.* (ETMC), PoS **LAT2009**, 145 (2009), arXiv:0910.3309.
- [21] J. Zanotti (QCDSF), private communication.
- [22] C. Alexandrou *et al.* (ETMC), in preparation.
- [23] T. Yamazaki *et al.* (RBC-UKQCD), Phys. Rev. D **79**, 114505 (2009).
- [24] A. Ali Khan *et al.* (QCDSF), Phys. Rev. D **74**, 094508 (2006).
- [25] T. R. Hemmert, M. Procura and W. Weise, Phys. Rev. D **68**, 075009 (2003).
- [26] S. N. Syritsyn *et al.* (LHPC), Phys. Rev. D **81**, 034507 (2010).
- [27] S. Capitani, M. Della Morte, B. Knippschild and H. Wittig, arXiv:1011.1358 [hep-lat].
- [28] T. R. Hemmert and W. Weise, Eur. Phys. J. A **15**, 487 (2002); M. Göckeler *et al.*, Phys. Rev. D **71**, 034508 (2005).
- [29] M. Göckeler *et al.* (QCDSF-UKQCD), PoS **LATTICE2008**, 138 (2008).
- [30] C. Alexandrou *et al.* (ETMC), PoS **LAT2009**, 136 (2009); T. Korzec, private communication.
- [31] D. B. Renner, PoS **LAT2009** (2009), arXiv:1002.0925.
- [32] D. Arndt, M. Savage, Nucl. Phys. **A697**, 429 (2002); W. Detmold, W. Melnitchouk, A. Thomas, Phys. Rev. D **66**, 054501 (2002).
- [33] C. N. Papanicolas, Eur. Phys. J. A **18**, 141 (2003).
- [34] C. Alexandrou *et al.*, PoS **LAT2009**, 156 (2009), arXiv:0910.5617; C. Alexandrou, Th. Leontiou, J. W. Negele and A. Tsapalis, Phys. Rev. Lett. **98**, 052003 (2007).
- [35] C. Alexandrou *et al.*, Phys. Rev. D **79**, 014507 (2009); Nucl. Phys. **A825**, 115 (2009).
- [36] C. Alexandrou *et al.*, PoS **Lattice 2010**, 141 (2010), arXiv:1011.3233.